

Resistivity of Rotated Graphite–Graphene Contacts

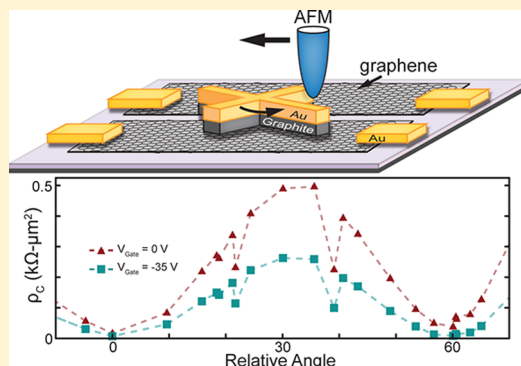
Tarun Chari,[†] Rebeca Ribeiro-Palau,[‡] Cory R. Dean,[‡] and Kenneth Shepard^{*,†}

[†]Department of Electrical Engineering and [‡]Department of Physics, Columbia University, New York, New York 10027, United States

Supporting Information

ABSTRACT: Robust electrical contact of bulk conductors to two-dimensional (2D) material, such as graphene, is critical to the use of these 2D materials in practical electronic devices. Typical metallic contacts to graphene, whether edge or areal, yield a resistivity of no better than $100 \text{ } \Omega \text{ } \mu\text{m}$ but are typically $>10 \text{ k}\Omega \text{ } \mu\text{m}$. In this Letter, we employ single-crystal graphite for the bulk contact to graphene instead of conventional metals. The graphite contacts exhibit a transfer length up to four-times longer than in conventional metallic contacts. Furthermore, we are able to drive the contact resistivity to as little as $6.6 \text{ } \Omega \text{ } \mu\text{m}^2$ by tuning the relative orientation of the graphite and graphene crystals. We find that the contact resistivity exhibits a 60° periodicity corresponding to crystal symmetry with additional sharp decreases around 22° and 39° , which are among the commensurate angles of twisted bilayer graphene.

KEYWORDS: Graphene, graphite, contact resistivity, commensurate angles



Electron transport through the two-dimensional (2D) van der Waals materials, such as graphene and the related transition metal dichalcogenides, remains limited by inefficient charge carrier injection from bulk contacts. Consequently, reducing contact resistance is critically important to device performance. For example, in graphene field effect transistors (GFETs), a high contact resistance is manifested as diminished on-current, transconductance, and output resistance.¹ These effects become increasingly significant with decreasing channel length, which causes the contact resistance in many cases to become equal to or greater than the channel resistance. For GFETs with channels lengths below $1 \text{ } \mu\text{m}$, a contact resistivity of better than $10 \text{ } \Omega \text{ } \mu\text{m}$ is required for the contact resistance to be less than 10% of the channel resistance.² Metallic contacts formed on the surface of graphene (so-called top, or areal, contacts) yield a wide range of contact resistivities from $100 \text{ } \Omega \text{ } \mu\text{m}$ to $>10 \text{ k}\Omega \text{ } \mu\text{m}$.^{3–5} It has been shown that the length over which current is injected into the graphene channel from the metallic top contacts (known as the transfer length, L_T) is $\sim 200 \text{ nm}$.^{6–8} Therefore, the contact resistance of metallic contacts with a length longer than L_T will only vary with the width of the channel. Consequently, contact resistivities are often cited in the width normalized units of $\Omega \text{ } \mu\text{m}$. Edge contacts have also been employed, which have delivered contact resistivities as low as $100 \text{ } \Omega \text{ } \mu\text{m}$.⁵

Efforts have been made to improve the contact resistivity of areal contacts by manipulating the graphene under the metal and varying the contact metal. For example, exposing the graphene to a mild O_2 plasma yields an order of magnitude improvement in the contact resistivity.⁹ More reproducible and reliable techniques include exposure to ultraviolet–ozone, bombardment with CO_2 clusters, and discriminately etching segments of the contact area.^{3,10,11} Among these techniques,

the latter have yielded the lowest contact resistivity of $125 \text{ } \Omega \text{ } \mu\text{m}$.¹¹ Varying the contact metal also impacts the contact resistivity, although work function mismatch does not appear to play a significant role^{9,12} since it has been shown that metals poorly wet the hydrophobic graphene surface, which leads to delamination.⁹ Also, it is hypothesized that metals with smaller grain sizes lead to a more uniform contact area and, therefore, a lower contact resistance.¹²

Here, we consider the use of graphite as the contact metal to graphene. Graphite has the advantage of being a bulk van der Waals material with identical crystal structure to graphene. As a result, the contact interface can be made atomically smooth.^{5,13,14} Moreover, integration of graphite contacts to the graphene surface by mechanical assembly avoids any concern about contamination at the interface that results from conventional nanofabrication techniques.⁵ Finally, graphite and graphene have similar work functions, which should minimize contact doping, making graphite attractive as an ambipolar contact metal. Many of these advantages have been demonstrated in other 2D materials such as niobium diselenide and molybdenum disulfide;^{15,16} however, less well understood is the effect of rotational misalignment across the device. Experimental studies of rotationally incommensurate graphene structures, including graphene on highly ordered pyrolytic graphite¹⁷ and twisted bilayer graphene (assembled from two rotationally mismatched graphene layers), consistently report that for general twist angles, transport is at least partially suppressed across the junction.^{17–21} Moreover, several theoretical efforts have suggested that interesting commensu-

Received: April 22, 2016

Revised: May 29, 2016

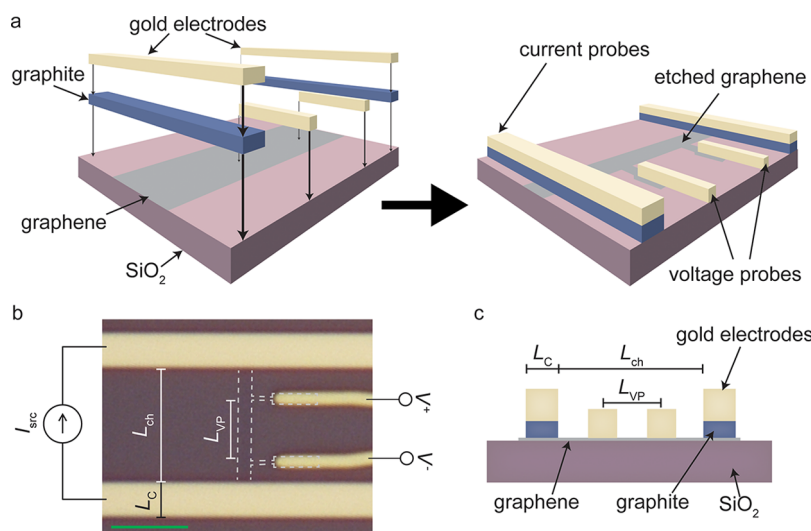


Figure 1. Device fabrication and experimental setup. (a) Graphite and graphene are exfoliated on separate SiO_2 on Si substrates. Metal contacts are evaporated (by e-beam deposition) onto the graphite, and then the graphite is etched using the metal as an etch mask. The graphite contacts are then lifted from its substrate and transferred onto the graphene using a dry transfer process. Next, metallic voltage probes are evaporated on the graphene. Finally, the graphene is then etched to form a $1\ \mu\text{m}$ wide channel length. (b) An optical image (scaled bar is $5\ \mu\text{m}$) of a typical device. The graphene is outlined in white. We define L_{ch} as the distance between the current probes, L_{vp} as the distance between the voltage probes, and L_{c} as the contact length. A $100\ \text{nA}$ current (I_{src}) is biased across the current probes and the voltage drop ($V^+ - V^-$) is measured across L_{vp} . For all devices fabricated in this way, L_{vp} and L_{ch} are 4.75 ± 0.25 and $7\ \mu\text{m}$, respectively. (c) A schematic cross-section of the final device with L_{ch} , L_{vp} , and L_{c} defined as in panel b.

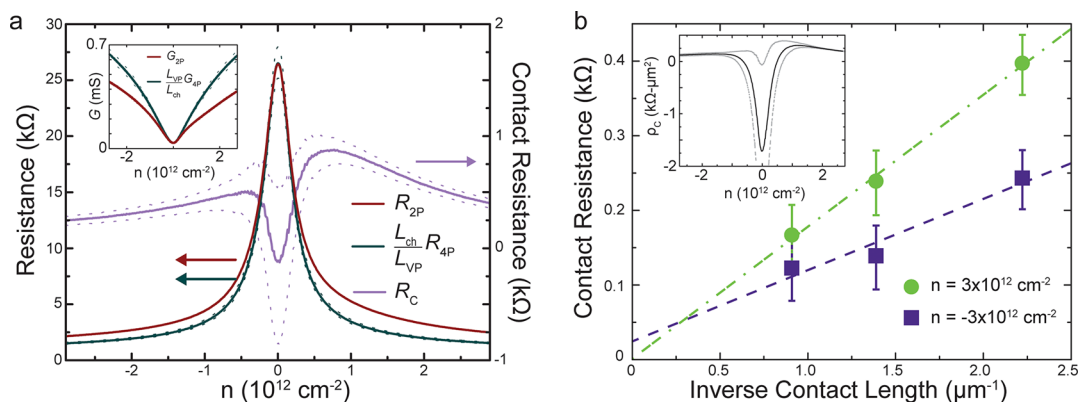


Figure 2. Experimental measurement. (a) The R_{2p} , $(L_{\text{ch}}/L_{\text{vp}})R_{4p}$, and R_{c} of the $0.45\ \mu\text{m}$ contact length device. R_{c} (solid purple curve) is half the difference between R_{2p} (solid red curve) and $(L_{\text{ch}}/L_{\text{vp}})R_{4p}$ (dashed green curve). The dotted curves represent the error induced from $L_{\text{vp}} = 4.75 \pm 0.25\ \mu\text{m}$. We observe a negative contact resistance around the charge neutrality point due to contact doping of the graphene channel near the contacts. The inset shows the two-terminal conductance ($\frac{1}{R_{2p}}$) and the scaled four-terminal conductance ($\frac{L_{\text{vp}}}{L_{\text{ch}}} \frac{1}{R_{4p}}$). The scaled four-terminal conductance shows electron hole symmetry, whereas the two-terminal conductance reveals an asymmetry due to an asymmetry in the contact resistivity. (b) The contact resistance, R_{c} , is inversely proportional the contact length, L_{c} , until L_{c} becomes larger than the transfer length, L_{T} . The constant of proportionality is the areal contact resistivity, ρ_{c} in units of $\Omega\ \mu\text{m}^2$. Here we plot the calculated R_{c} versus L_{c}^{-1} at high hole (purple squares) and holes of $177 \pm 2\ \Omega\ \mu\text{m}^2$ and $95 \pm 2\ \Omega\ \mu\text{m}^2$, respectively. We also observe a nonzero intercept, which is due to small series resistances that do not scale with contact area such as the metal-graphite contact resistance ($\sim 10\ \Omega$) and the c -axis resistivity of graphite. Inset: ρ_{c} (solid line) as a function of carrier density shows a relatively constant resistivity at high densities and a sharply negative resistivity around charge neutrality. The error (dashed line) indicates that the high-density resistivity is robust and the low-density resistivity is unreliable.

rate phases may emerge at precisely defined angles giving rise to a new class of interfacial states.^{22,23}

In this Letter, we report measurement of the resistivity across a graphene and bulk graphite junction as a function of contact area and relative twist angle. At an arbitrary angle, we find that the contact resistance scales with area, and we deduce a transfer length, L_{T} , several-times longer than that observed for conventional metallic areal contacts.^{6–8} We also fabricate a novel device structure in which we can dynamically vary the

rotational angle while measuring the resistance of the junction, which allows a systematic map of the resistivity spanning a full period of commensurate to incommensurate rotation angles. We find that the resistivity is a strong function of crystal orientation with 60° periodicity. At the zero angle, the contact resistivity is no more than $6.6\ \Omega\ \mu\text{m}^2$, which provides the lowest ever reported contact resistivity to graphene, and increases more than an order of magnitude at 30° . Additionally, sharp conductance peaks are observed around 22° and 39° ,

which are among the commensurate angles theoretically predicted for twisted bilayer graphene.^{22,23}

To fabricate these devices, we begin with a single, mechanically exfoliated graphite (21 nm thick) crystal on 285 nm SiO₂ on Si substrates. We then evaporate metal contacts onto the graphite (1 nm:50 nm Cr/Au) and etch the graphite using the metal as an etch mask. The etched graphite structure is then mechanically transferred using the dry transfer process.⁵ Since the area of the constituent crystals is large (>100 μm²), many pairs of contacts can be etched from the graphite and transferred simultaneously onto the graphene to ensure that the crystallographic orientation is the same for all contact pairs. It is important to note that the graphene at this time has not been lithography processed; therefore, the graphite–graphene interface is pristine.⁵ After transfer, we evaporate voltage probes, leads, and probe pads (1 nm:100 nm Cr/Au) and then etch the graphene into 1 μm wide channels (Figure 1). Three characteristic lengths are defined for these structures. We denote the distance between the graphite contacts as the channel length, L_{ch} . In addition, we define the distance between the voltage probes as L_{VP} . Finally, we define the length of the graphite contact as L_{C} , all shown in Figure 1, panel c.

Electrical measurements are performed (at room temperature) by current biasing the device (100 nA) and measuring the voltage drop across the graphene (four-terminal) or across the entire device (two-terminal), yielding both four-terminal resistance ($R_{4\text{P}}$) and two-terminal resistance ($R_{2\text{P}}$) values. We vary the carrier density in the graphene from $-3 \times 10^{12} \text{ cm}^{-2}$ to $+3 \times 10^{12} \text{ cm}^{-2}$ by modulating the silicon back gate voltage from -40 V to $+40 \text{ V}$. The contact resistance (R_{C}) is determined by subtracting $R_{4\text{P}}$, scaled by the ratio of $L_{\text{ch}}/L_{\text{VP}}$, from $R_{2\text{P}}$ as $2R_{\text{C}} = R_{2\text{P}} - \frac{L_{\text{ch}}}{L_{\text{VP}}} R_{4\text{P}}$ (Figure 1b). In all devices, the nominal $L_{\text{ch}}/L_{\text{VP}}$ ratio is 1.47 with L_{ch} of 7 μm and L_{VP} of $4.75 \mu\text{m} \pm 0.25 \mu\text{m}$, where this variance comes from the width of the voltage probes.

To explore the areal dependency on the contact resistance, we fabricated three devices with contact lengths of 0.45 μm, 0.72 μm, and 1.1 μm. These devices were fabricated using the same graphite and graphene crystals and, therefore, have the same, albeit unknown, relative crystal orientation (see Supporting Information). $R_{2\text{P}}$ and $(L_{\text{ch}}/L_{\text{VP}})R_{4\text{P}}$ for $L_{\text{C}} = 0.45 \mu\text{m}$ are shown in Figure 2, panel a as a function of sheet density in the channel. The mobility and intrinsic doping for the graphene channel can be determined by fitting the scaled four-terminal resistance to the expression $R_{4\text{P}} = W/L_{\text{ch}}q\mu\sqrt{n_0^2 + n^2}$, where W is the channel width, μ is the carrier mobility, n_0 is the intrinsic doping, n is the carrier density, and q is the elementary charge. All three devices yield intrinsic doping, n_0 , of $\sim 1.4\text{--}1.5 \times 10^{11} \text{ cm}^{-2}$ and carrier mobilities, μ , of $9000\text{--}10\,000 \text{ cm}^2 \text{ V}^{-1} \text{ s}^{-1}$. We also note that $R_{4\text{P}}$ is symmetric with carrier density across all three devices (Figure 2a, inset).

The calculated value of R_{C} for the $L_{\text{C}} = 0.45 \mu\text{m}$ device is also shown in Figure 2, panel a. At high density, the contact resistance is $250 \pm 40 \Omega$ and $400 \pm 40 \Omega$ for holes and electrons, respectively. Around the charge neutrality point, we calculate a negative contact resistance, which has also been reported elsewhere and is an artifact of contact-induced doping of the graphene in a region near the contact.²⁴ The four-terminal measurement does not include this region and, therefore, leads to an overestimation in the resistance of the

channel around the charge neutrality point. We restrict further analysis of the contact resistance to the high-density regime where the impact of this artifact is negligible.

The areal contact resistivity, ρ_{C} , varies linearly with the inverse of the contact length, $R_{\text{C}} = \frac{\rho_{\text{C}}}{WL_{\text{C}}}$. We, therefore, plot R_{C} as a function of $1/L_{\text{C}}$ in Figure 2, panel b. We observe that R_{C} at a carrier density of $n = \pm 2.75 \times 10^{12} \text{ cm}^{-2}$ does vary linearly with $1/L_{\text{C}}$ indicating that contact resistance depends on the total contact area in contrast to metallic top contacts, which only depend on the width of the graphene channel.^{6–8} We extract a contact resistivity for electrons and holes of $177 \pm 2 \Omega \mu\text{m}^2$ and $95 \pm 2 \Omega \mu\text{m}^2$, respectively. The transfer length, L_{T} , can be calculated from $L_{\text{T}} = \sqrt{\frac{\rho_{\text{C}}}{\rho_{\text{g}}}}$, where ρ_{C} is the contact

resistivity, and ρ_{g} is the graphene resistivity under the contact. While we know ρ_{g} will be influenced by contact doping, we cannot determine it directly and instead approximate it by the value we calculate away from the contacts from $R_{4\text{P}}$ according to $\rho_{\text{g}} = \frac{W}{L_{\text{VP}}} R_{4\text{P}}$. At high density, the estimated hole (electron) transfer length is 713 ± 7 (886 ± 5) nm, which is consistent with the observed area scaling in Figure 2, panel b. Comparatively, the transfer length for metallic top contacts is $\sim 200 \text{ nm}$.

Since graphite and graphene are both honeycomb lattice structures, we expect ρ_{C} to depend on the relative crystal orientation. Theoretical predictions indicate that the interlayer transport of a twisted bilayer structure exhibits a strong angle dependence.^{22,23} To measure the graphite contact resistivity as a function of the relative angle to the graphene, we fabricate the device depicted in Figure 3, panel a. The fabrication process is very similar to that used for the devices shown in Figure 2. The graphite is etched into a cross structure (with a protective metallic cap) and transferred to electrically connect two narrowly spaced, 2-μm-wide graphene strips. Metallic current and voltage probes are then evaporated onto the ends of the graphene strips to allow a four-terminal resistance measurement of just the graphite–graphene contact area (Figure 3a). Unlike the previous devices shown in Figure 2, here the measured four-terminal resistance ($R_{4\text{T}} = \frac{V^+ - V^-}{I_{\text{src}}}$, with I_{src} , V^+ , and V^- defined in Figure 3, panel a), includes two graphite–graphene contacts and the bulk graphite resistance. We calculate the contact resistivity, ρ_{C} , as $\rho_{\text{C}} = (1/2)R_{4\text{T}}A$, where A is the angle-dependent area of one contact. This calculation ignores a series resistance contribution from the bulk graphite over the gap between the graphene strips. At a gap spacing of 300 nm, we estimate this contribution to be at most 6 Ω for our device geometry (see Supporting Information). At the smallest values of ρ_{C} , this can result in an error as large as 40%, while at the highest values of ρ_{C} , this error is less than 1.5%. Additionally, small (<100 nm) translations in the graphite contact during some rotations lead to an area mismatch between the contacts on each graphene strip. We estimate this angle-dependent contact area variance to be less than $0.09 \mu\text{m}^2$, which results in an approximately 7% error in our calculated ρ_{C} .

Rotation of the graphite contact is achieved by using an atomic force microscope (AFM). An orthogonal force is applied on the extremities of the graphite cross, which induces rotation about the center of the cross (see Supporting Information). Figure 3, panel b shows AFM images of the

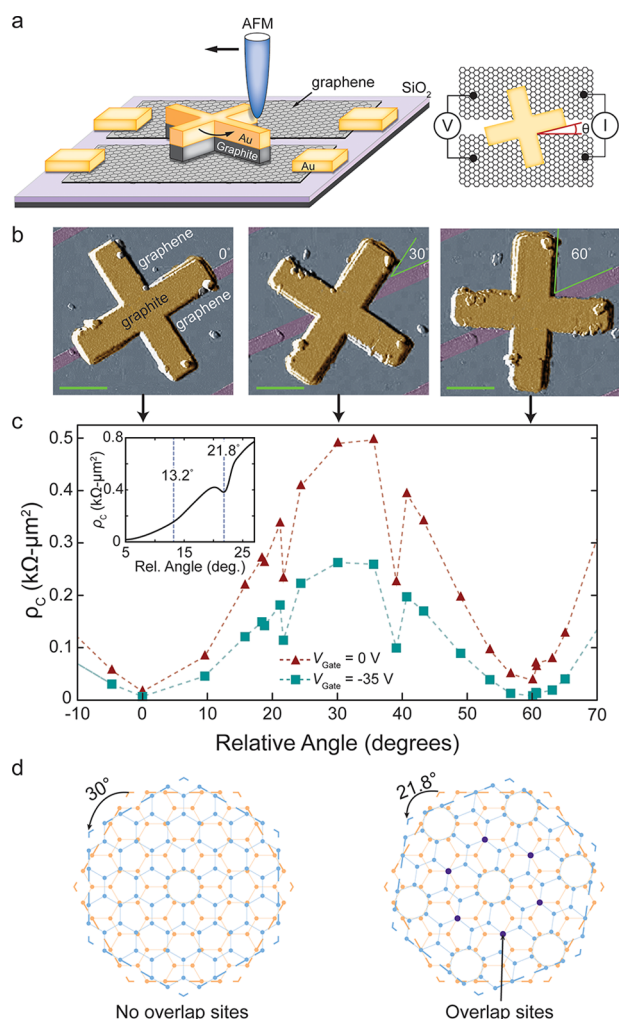


Figure 3. Crystal orientation dependence. (a) Schematic diagram of the experimental setup to probe the orientation dependency on the contact resistance. The graphene is etched into $2\ \mu\text{m}$ wide strips separated by $300\ \text{nm}$. Graphite is etched into a cross shape using a metallic mask. The metallic cap serves to protect the graphite during the rotation and does contribute to electrical conduction. Metallic current and voltage probes are evaporated onto the ends of the graphene. A current is biased between two ends of the graphene strips, while the other ends serve as voltage probes. (b) AFM images of the graphite contact demonstrating successful rotation through 60° (scaled bar is $1\ \mu\text{m}$). The angle is measured from these images relative to the graphene strips. (c) The angle dependence on the contact resistance reveals three striking features. First, the resistance exhibits a 60° periodicity, which matches the rotational symmetry of the constituent crystals. Second, the resistance varies from $6.6\ \Omega\ \mu\text{m}^2$ to $260\ \Omega\ \mu\text{m}^2$ at high hole density. Finally, sharp decreases in the contact resistance are observed around 22° and 39° , which correspond to two of the six commensurate angles of twisted bilayer graphene: 13.2° , 21.8° , 27.8° , 32.2° , 38.2° , and 46.8° . Inset: A dynamic measurement was performed (on a separate device) where the electrical measurement is performed while graphite contact is rotated. We observe the local resistivity minimum around 21.8° , but there is no minimum present at 13.2° . (d) Extended zone Fermi circles of twisted bilayer graphene. The dots represent the Fermi circles, and the top layer (blue) Fermi circles is rotated relative to the bottom layer (orange) of Fermi circles. When the relative rotational angle is 30° , there is no overlap of the Fermi circles, and the resistivity is large. When the angle is 21.8° , there is precise overlap at some points between the Fermi circles of the top and bottom layers, and the resistivity exhibits a local minimum. This overlap is only observed at the commensurate angles.

graphite cross at different angles. At each rotation, we calculate R_{meas} while the back gate is varied.

The calculated resistivity is shown in Figure 3, panel c for high hole and charge neutral densities. The resistivity exhibits a 60° periodicity with the relative angle, which precisely matches the hexagonal symmetry of the respective crystal lattices. At 0° and 60° , the resistivity at high hole carrier density is $6.6\ \Omega\ \mu\text{m}^2$ and $7.8\ \Omega\ \mu\text{m}^2$, respectively, which, within the error resolution of our measurement, is identical. The 0° angle coincides with the straight edge of the graphite and graphene. This is because during fabrication, the bulk crystals were etched relative to the straight edges observed in the optical micrograph. We expect that straight edges of the bulk crystals correspond to armchair or zigzag terminations of the lattice, which in turn define the bulk crystal orientation. Consequently, the etched structures will preserve this crystallinity relative to their etched straight edges (to within a spatial error induced by e-beam lithography). The fact that the resistance minimum occurs when the straight edges of the etched crystals are aligned implies that the edge terminations of the corresponding bulk crystals were the same (both armchair or both zigzag). In the case where the bulk crystal edge terminations are opposite, we would expect a resistance maximum.

Moreover, because of the contribution of the bulk graphite, this contact resistivity, while already less than $10\ \Omega\ \mu\text{m}^2$, represents an upper bound. At 30° , we observe a contact resistivity maximum, which at the same hole density is $260\ \Omega\ \mu\text{m}^2$, a 40-fold increase from the value at the minimum. In this calculation, we assume the entire area of the contact contributes to current injection. In reality, only the area up to the transfer length will contribute to current injection. However, since the contact resistivity will change as a function of angle, the transfer length will also change as a function of angle, which will render a precise calculation of the contact resistivity impossible. Nonetheless, our calculated resistivity remains an upper bound since it overestimates the area over which current is injected. We note also that the devices in Figure 2, where the relative crystal orientation is unknown, showed a hole resistivity of $95\ \Omega\ \mu\text{m}^2$, which is within the range of resistivities attained over all rotational orientations. The effects of performing a nonlocal measurement are also negligible as evinced by the experimental data. These nonlocal effects should manifest with a 90° period (owing to the symmetry of the graphite contact) convolved with the 60° periodicity of the resistivity and result in an asymmetric measurement about 30° . However, the observed resistivity is symmetric, which implies that any nonlocal effects are negligible.

In addition to this overall periodicity, we observe finer structure in the resistivity, in particular, a decrease in resistivity around 22° and 39° . These angles correspond to two of the six theoretically predicted, large angle commensurate states of twisted bilayer graphene: 13.2° , 21.8° , 27.8° , 32.2° , 38.2° , and 46.8° .²³ This precision in determination of the commensurate angles in Figure 3, panel b indicates that the graphite–graphene crystal lattices are in fact aligned at 0° and fully misaligned at 30° . We also observe a slight difference in the resistivity between the 22° and 39° angles of $114\ \Omega\ \mu\text{m}^2$ and $99.5\ \Omega\ \mu\text{m}^2$, respectively.

To understand why the resistance decreases at the 22° and 39° commensurate angles, it is useful to examine the Fermi circles of two graphene crystals at these angles. For example, Figure 3, panel d shows the extended zone of the Fermi circles rotated by 30° and 21.8° . At 30° , there is no overlap of the

Fermi circles, and the layers are fully momentum mismatched. Electrons therefore cannot tunnel between the layers without involving some phonon scattering.¹⁷ At 21.8°, some Fermi surfaces overlap, and therefore, some amount of resonant interlayer tunneling becomes possible. Close examination of Figure 3, panel d reveals that overlap sites are from the K point in one layer to the K' point in the other layer (intervalley). In general, there are two distinct transport types in commensurate rotations: intravalley and intervalley transport. The overlap sites are intervalley at 13.2°, 21.8°, and 32.2° and are intravalley at 27.8°, 38.2°, and 46.8°. This may give rise to the observed resistivity mismatch between the 22° and 39°, as we expect intravalley transport to yield lower resistivity than intervalley transport.

In Figure 3, panel c, pronounced resistance minimum is observed only for the 21.8° commensurability angle. To more carefully examine this effect, we performed a dynamic measurement (on a separate device). A −35 V back gate was applied, and R_{4T} was measured while the AFM tip rotated the graphite contact. In this way, we were able to continuously measure R_{4T} from 5° to 25° (see left inset in Figure 3c). While we reproduce the resistance minimum at 21.8°, we do not observe the same characteristic resistivity drop at the 13.2° commensurate angle, despite the fact that both angles have intervalley overlap site. This result is consistent with the 21.8° and 13.2° conductance peaks calculated theoretically to be different by several orders of magnitude.²³ This can be understood in part from the fact that the unit cell of the 13.2° superlattice is ~2.7-times larger than the superlattice at 21.8° and therefore corresponds to fewer total commensurability sites over the whole device. Consequently, it may be that the relative impact of the overlap sites at 13.2° is obscured due to room temperature smearing.^{17,18}

In conclusion, we observe the lowest ever reported contact resistivity to graphene of $6.6 \Omega \mu\text{m}^2$ using single-crystal, bulk graphite. The estimated transfer length of the graphite contacts is >700 nm, which is more than 3.5-times longer than for metallic top contacts. Furthermore, the graphite–graphene contact resistivity is similar for both electrons and holes, which improves ambipolar device operation. We also observe that this resistivity shows a strong dependence on the relative orientation of the graphite and graphene crystals and in particular find first evidence of enhanced conductance across the junction at nonzero commensurability angle. The crystal orientation dependence on the contact resistance is a feature we expect to be observed in other 2D crystals. Finally, the capability to dynamically vary the crystallographic orientation makes it also possible to precisely tune the band structure in devices assembled from 2D crystals and provides sufficient resolution to test the many theoretical predictions of exotic states emerging in rotationally ordered mixed-layer heterostructures.

■ ASSOCIATED CONTENT

● Supporting Information

The Supporting Information is available free of charge on the ACS Publications website at DOI: 10.1021/acs.nanolett.6b01657.

Metal–graphite contact resistance, device fabrication, measuring the relative crystal orientation, and rotating the graphite contact (PDF)

■ AUTHOR INFORMATION

Corresponding Author

*E-mail: shepard@ee.columbia.edu.

Notes

The authors declare no competing financial interest.

■ ACKNOWLEDGMENTS

We thank G. Mele for helpful discussions. C.R.D. acknowledges partial support for this work by the NSF Grant No. DMR-1420634. K.S. acknowledges support from the SRC-NRI INDEX Center.

■ REFERENCES

- (1) Parrish, K. N.; Akinwande, D. *Appl. Phys. Lett.* **2011**, *98* (18), 16–19.
- (2) Chari, T.; Meric, I.; Dean, C.; Shepard, K. *IEEE Trans. Electron Devices* **2015**, *62* (12), 4322–4326.
- (3) Li, W.; Hacker, C. A.; Cheng, G.; Liang, Y.; Tian, B.; Hight Walker, A. R.; Richter, C. A.; Gundlach, D. J.; Liang, X.; Peng, L. *J. Appl. Phys.* **2014**, *115* (11), 2012–2017.
- (4) Leong, W. S.; Gong, H.; Thong, J. T. L. *ACS Nano* **2014**, *8* (1), 994–1001.
- (5) Wang, L.; Meric, I.; Huang, P. Y.; Gao, Q.; Gao, Y.; Tran, H.; Taniguchi, T.; Watanabe, K.; Campos, L. M.; Muller, D. A.; Guo, J.; Kim, P.; Hone, J.; Shepard, K. L.; Dean, C. R. *Science* **2013**, *342* (6158), 614–617.
- (6) Franklin, A. D.; Han, S.-J.; Bol, A. a.; Haensch, W. *IEEE Electron Device Lett.* **2011**, *32* (8), 1035–1037.
- (7) Xu, H. H.; Wang, S.; Zhang, Z.; Wang, Z.; Xu, H. H.; Peng, L.-M. *Appl. Phys. Lett.* **2012**, *100* (10), 103501.
- (8) Nagashio, K.; Nishimura, T.; Kita, K.; Toriumi, A. *Appl. Phys. Lett.* **2010**, *97* (14), 143514.
- (9) Robinson, J. a.; LaBella, M.; Zhu, M.; Hollander, M.; Kasarda, R.; Hughes, Z.; Trumbull, K.; Cavallero, R.; Snyder, D. *Appl. Phys. Lett.* **2011**, *98* (5), 053103.
- (10) Gahng, S.; Ho Ra, C.; Jin Cho, Y.; Ah Kim, J.; Kim, T.; Jong Yoo, W. *Appl. Phys. Lett.* **2014**, *104* (22), 2012–2016.
- (11) Smith, J. T.; Franklin, A. D.; Farmer, D. B.; Dimitrakopoulos, C. D. *ACS Nano* **2013**, *7* (4), 3661–3667.
- (12) Watanabe, E.; Conwill, A.; Tsuya, D.; Koide, Y. *Diamond Relat. Mater.* **2012**, *24*, 171–174.
- (13) Cui, X.; Lee, G.-H.; Kim, Y. D.; Arefe, G.; Huang, P. Y.; Lee, C.; Chenet, D. A.; Zhang, X.; Wang, L.; Ye, F.; Pizzocchero, F.; Jessen, B. S.; Watanabe, K.; Taniguchi, T.; Muller, D. A.; Low, T.; Kim, P.; Hone, J. *Nat. Nanotechnol.* **2015**, *10* (6), 534–540.
- (14) Haigh, S. J.; Gholinia, A.; Jalil, R.; Romani, S.; Britnell, L.; Elias, D. C.; Novoselov, K. S.; Ponomarenko, L. A.; Geim, A. K.; Gorbachev, R. *Nat. Mater.* **2012**, *11* (9), 764–767.
- (15) Lee, G.; Cui, X.; Kim, D.; Arefe, G.; Zhang, X.; Lee, C.; Ye, F.; Watanabe, K.; Taniguchi, T.; Kim, P.; Hone, J. *ACS Nano* **2015**, *9* (7), 7019–7026.
- (16) Tsen, A. W.; Hunt, B.; Kim, Y. D.; Yuan, Z. J.; Jia, S.; Cava, R. J.; Hone, J.; Kim, P.; Dean, C. R.; Pasupathy, A. N. *Nat. Phys.* **2015**, *12*, 208–212.
- (17) Luican, A.; Li, G.; Reina, A.; Kong, J.; Nair, R. R.; Novoselov, K. S.; Geim, A. K.; Andrei, E. Y. *Phys. Rev. Lett.* **2011**, *106* (12), 126802.
- (18) Kim, Y.; Yun, H.; Nam, S. G.; Son, M.; Lee, D. S.; Kim, D. C.; Seo, S.; Choi, H. C.; Lee, H. J.; Lee, S. W.; Kim, J. S. *Phys. Rev. Lett.* **2013**, *110* (9), 096602.
- (19) Kim, C. J.; Sánchez-Castillo, A.; Ziegler, Z.; Ogawa, Y.; Noguez, C.; Park, J. *Nat. Nanotechnol.* **2016**, 1–6.
- (20) Sanchez-Yamagishi, J. D.; Taychatanapat, T.; Watanabe, K.; Taniguchi, T.; Yacoby, A.; Jarillo-Herrero, P. *Phys. Rev. Lett.* **2012**, *108* (7), 076601.
- (21) Chae, D. H.; Zhang, D.; Huang, X.; Von Klitzing, K. *Nano Lett.* **2012**, *12* (8), 3905–3908.

- (22) Mele, E. J. *Phys. Rev. B: Condens. Matter Mater. Phys.* **2010**, *81* (16), 1–4.
- (23) Bistrizter, R.; MacDonald, A. H. *Phys. Rev. B: Condens. Matter Mater. Phys.* **2010**, *81* (24), 245412.
- (24) Nouchi, R.; Saito, T.; Tanigaki, K. *J. Appl. Phys.* **2012**, *111* (8), 084314.